

EXTRA-LARGE EDDY SIMULATION FOR DELTA WINGS AND SPACE LAUNCHERS

K.M.J. de Cock, J.C. Kok, H. van der Ven, B.I. Soemarwoto, O.J. Boelens, B. Oskam
 National Aerospace Laboratory NLR, P.O. Box 90502, 1006 BM Amsterdam, The Netherlands

Keywords: *dynamic loads, large-eddy simulation, flight dynamics, vortex breakdown, base flow*

Abstract

Time-dependent flow phenomena can have a strong impact on performance and flight characteristics of aerospace vehicles and therefore play a crucial role in their design and operation. On modern high-performance fighter aircraft well-ordered leading-edge vortices are deliberately generated. Under specific operational conditions, the vortices break down and lose their well-ordered structure. As a result, highly dynamic flow can be impinging on downstream tail structural components, which may cause early fatigue or loss of the tail structure. In other cases, vortex breakdown is an important factor leading to uncommanded oscillatory motions of fighter aircraft, such as nose slice, wing rock and wing drop. For space launchers, an important challenge is to accurately assess dynamic external loads on the structural components of the space launcher, caused by massively separated flow.

In this paper, the impact of new turbulence modelling efforts on two of the above aerospace applications is explored. The new turbulence modelling logic is presented and demonstrated for vortex breakdown above a delta wing and for a space-launcher base flow.

1 Introduction

Fighter-aircraft design has been pushed towards the expansion of flight envelopes into extreme attitudes and aggressive manoeuvres with high angular rates. Potentially, the enhanced tactical agility increases air-combat exchange ratio. On

the other hand, severe stability and control problems can arise that increase the probability of departure from controlled flight.

Unfortunately, because of the highly non-linear aerodynamic phenomena involved [11], characterised by vortical flow and massive separation, predictive methods are not always able to reveal the onset and nature of the problems early in the design phase. Sometimes, a problem appears during a full-scale flight test. Continuing the program without solving the problem would put severe restriction on the aircraft performance, while pilots in operational squadrons would strongly object to artificial manoeuvre limits. On the other hand, the cost incurred to fix the problem can be very high. To keep the budget overshoot under control, fixes tend to be ad hoc and are applied without a sound basis of fundamental understanding of the physics concerned. A recent example is the problem encountered in the flight-test program of the F/A-18E/F. During transonic manoeuvres, the aircraft experienced an uncommanded lateral motion known as wing drop. As a consequence, quoted from [11], a significant amount of additional testing and engineering support was required to find a successful solution to the wing-drop problem. The fixes consisted of modifications to the leading-edge flap schedule and addition of a porous fairing at the wing-fold location. As a result of the wing-drop problem, a national program was initiated in the United States, leading to extensive experimental and computational studies of abrupt wing stall [4, 7, 20].

Encountering a stability and control problem

during the operational phase is even more severe than during the flight-test phase. Eventually, the problem can lead to accidents with loss of aircraft and pilot. An example can be found in [1], describing the loss of an F-16 after an out-of-control roll behaviour at a high angle of attack.

The flight dynamics under consideration refer to the characteristics of departure susceptibility, departure motion, and possible recovery from departure. The characteristics depend on the aerodynamic properties and their variation with aircraft attitudes, as well as on the inertial and geometric properties of the aircraft. Based on the physics modelled, three levels of flight-dynamics assessment can be identified.

At Level-1, the assessment is based on the values and derivatives of the aerodynamic force and moment coefficients at representative steady conditions, which are obtained from flight tests, wind-tunnel experiments, or CFD computations. For example, the longitudinal characteristic for aircraft featuring relaxed static stability is evaluated using a minimum nose-down control parameter [12]. The lateral-directional characteristics are commonly evaluated based on the criteria expressed in terms of the Lateral Control Departure Parameter, and the Synchronous Roll-Yaw Parameter [18, 3]. These parameters can give first estimates of the departure boundaries. For aggressive manoeuvres, however, a level-1 assessment may become unacceptably inaccurate [2].

At Level-2, the assessment is based on simulations using an aerodynamic model, basically a set of linear expansions of the equation of motion around points covering (part of) the flight envelope. The aerodynamic data at these points are also obtained from flight tests, wind-tunnel experiments, or CFD computations. A manoeuvre is defined in terms of a starting condition and a control input schedule for a certain period of time. The simulation provides the time responses of the aircraft. Departures can be identified as incipient temporal excursions in the angle of attack, sideslip, and rotational rates [2, 5]. However, a level-2 approach is still limited, among others because the aerodynamic data can only be obtained for a limited number of points. When a

prolonged excursion occurs, the simulation may enter a domain where there is no data available, and an extrapolation is usually employed. Obviously, the validity of an extrapolated model is questionable.

At Level-3, the non-linear fluid, flight and structural dynamics are coupled in the non-linear equations of motion for flexible bodies. The resulting aero-servo-elasticity simulation capability, which accounts for the non-linearities throughout the simulation, ensures an accurate flight-dynamics assessment. Another important advantage is that a level-3 assessment can be performed well into a domain where a flight test would incur too much safety hazards.

The research presented in this paper is a step towards pursuing the high-fidelity capability to perform a level-2 and 3 flight mechanics assessment. Two aspects are essential: (i) the capability of the CFD method to capture details of the flow physics, and (ii) the coupling of the flow equations and the equations of motion. The first aspect is addressed in research efforts to model vortical flow phenomena with higher fidelity, and is the focus of this paper. The second aspect is for instance treated in [16].

Another aerospace application is the assessment of space-launcher base-flow dynamic external loads. After the failure of the inaugural launch of the upgraded Ariane 5 ECA on Wednesday December 11, 2002, the inquiry board stated that one of the most probable causes for this failure consisted of a ‘non-exhaustive definition of the design loads, combined with a combination of various stress factors during the flight.’ Among the load cases is the dynamic external load on the Vulcain nozzle caused by the massively separated flow from the base of the Ariane 5 space launcher. The capability to accurately compute such a dynamic external load case would be of great value for the (re)design of the engine.

Efforts to simulate the flows mentioned above and the associated dynamics based on the Reynolds-Averaged Navier-Stokes (RANS) equations have revealed several problems [15]. For separated flows, the frequency range of the

dominant flow structures cannot be discriminated from the turbulence spectrum, a basic assumption of RANS simulations. Moreover, the RANS equations incorporate too much dissipation in the flow separation areas to resolve small scales.

On the other hand, Large Eddy Simulation for realistic geometries and Reynolds numbers is years off due to the inherently large computational complexity as a result of the resolution required close to solid boundaries.

A new composite formulation for the simulation of dynamic flows, called ‘Extra-Large Eddy Simulation’ (X-LES), was first presented in [6]. It applies a non-zonal treatment to combine RANS-type turbulence models and Large Eddy Simulation (LES) type turbulence models, using a single turbulent kinetic energy equation.

In the next section the composite formulation of the X-LES model is described, and applications are discussed in Section 3. These applications are linked to the prediction of vortex breakdown around a delta wing (Section 3.1), and the computation of dynamic external loads in the base region of a space launcher (Section 3.2). Finally, conclusions are drawn.

2 X-LES model

2.1 Points of departure

In recent years, hybrid RANS–LES methods have become a focal point, aiming for increased physical fidelity over RANS without the costs of a full LES. One such a method was followed by Spalart [17], named Detached Eddy Simulation (DES), in which a hybrid turbulence model, based on the Spalart–Allmaras model, was used that could switch between RANS and LES modes, depending on the wall distance and the mesh size.

In the X-LES model, a composition of the RANS and LES formulations is formed which uses a single equation of the turbulent kinetic energy. In this section, a foundation for this model is presented based on time filters. The main benefit of this foundation is that a single definition of the filtered flow states is used in the entire flow

domain. Depending on the time scales in the flow different turbulence models are used. The basic idea is to use RANS-type turbulence models in those regions where the assumption of separation of scales (SoS) is valid, and LES-type turbulence models otherwise.

Using the standard RANS and LES formulations, it is difficult to define a smooth transition between the RANS and LES filters. The RANS filter is based on an ensemble average, which is commonly replaced by a time average, where the time interval is sufficiently large to filter out the smaller turbulent scales, but small enough to retain the relevant flow phenomena, based on the SoS assumption. LES filters usually are defined spatially. In standard hybrid RANS–LES methods these two filters are applied in the different regions, and hence the flow variables represent different quantities. In particular, the turbulent kinetic energy is defined differently in the different regions, which, at least theoretically, makes it difficult to couple the turbulent kinetic energies at the interface.

In an interesting paper, Pruett [13] investigates the use of temporal filters in LES. A drawback of temporal filters is that the subgrid stresses are no longer Galilean invariant, which causes a Doppler shift of the resolved wave numbers under a Galilean transformation [13]. In practice this means that in regions with different convection velocities, different scales are represented. However, in free-shear flows, where there is a common characteristic velocity, LES based on temporal filtering is appropriate.

In the X-LES formulation, only one temporal filter is used to define the filtered quantities, thus unifying RANS and LES in a single framework. The X-LES formulation is designed to apply a RANS turbulence model in the boundary layer, and a LES model in the separated regions, where the flow resembles free-shear flows and, hence, temporal filtering is appropriate.

The switch between RANS and LES turbulence models is based on the turbulence time scales. Whenever the turbulence time scales in the flow are too small to be resolved by the temporally filtered flow solution, the RANS turbu-

lence model is active, otherwise the LES turbulence model is active. As will be shown below, the switch is implemented in such a way that the switch to LES is performed when the SoS assumption of RANS is still valid. Theoretically, the last property precludes the necessity of inserting artificial turbulent statistics at the interface.

2.2 Design

The Navier–Stokes equations are filtered using a temporal filter. A set of equations is then obtained which has the same form as the standard LES equations when based on spatial filtering. The subgrid-scale (SGS) stress tensor, is modelled as follows: (a) In case of a clear separation of scales (characteristic turbulence time scales smaller than time-filter width), a RANS-type model can be used; in particular, the k – ω model is used here. (b) In case of no clear separation of scales, a LES-type model should be used; in particular, a k -equation model is used here. Both the RANS-type and the LES-type models are based on the Boussinesq hypothesis and employ an equation for the subgrid-scale kinetic energy k . A composition of the two models is formed, in which the k and ω equations are solved in the complete domain, but with the k equation switching to the LES-type formulation when necessary. In the composite SGS model, the eddy viscosity ν_t and the dissipation of subgrid kinetic energy ϵ are modelled as $\nu_t = \tilde{l}\sqrt{k}$ and $\epsilon = \beta_k k^{3/2}/\tilde{l}$, with \tilde{l} a suitable composite length scale ($\beta_k = 0.09$).

To determine when it is necessary to switch to the LES-type formulation, a characteristic turbulence time scale is needed that can be compared to the time-filter width Δ_t . The switch is intended to take place in the wake or in the outer part of the boundary layer. There, one can make use of the Taylor hypothesis: at a fixed location, fluctuations in time are dominated by the convection of turbulence by the mean velocity. Hence, the relevant turbulence time scale follows from the turbulence length scale and the mean velocity: $\tau = l/U_{\text{ref}}$ with $l = \sqrt{k}/\omega$ the turbulence length scale for the k – ω model and with U_{ref} a charac-

teristic mean velocity scale. When this time scale becomes of the same order as or larger than the filter width Δ_t , then the k equation should switch to the LES-type formulation.

To close the SGS model, the composite length scale \tilde{l} must be modelled, implementing the switch between the RANS-type and LES-type formulations. First, a composite time scale is formed as

$$\tilde{\tau} = \min\{\tau, C_1\Delta_t\}, \quad (1)$$

with C_1 a model constant. Multiplication with the reference velocity U_{ref} gives a composite length scale:

$$\tilde{l} = \min\{l, C_1\Delta\}, \quad (2)$$

with $\Delta = U_{\text{ref}}\Delta_t$. More details can be found in [6].

The Taylor hypothesis for the turbulence time scale is valid in those parts of the flow where a characteristic mean velocity scale is present. In the boundary layer we need a different argumentation to show that in RANS mode the SoS assumption remains valid. For this we have to demonstrate that the RANS time scale $t_{\text{RANS}} = 1/\omega$ is sufficiently smaller than the filter width Δ_t . Since in the boundary layer the RANS time scale goes to zero, this is satisfied in the inner boundary layer. If the flow remains turbulent away from the wall, the RANS time and length scales will grow, and eventually switch (1) will be activated and the LES model will be activated. If at this point the SoS assumption is still valid, one can safely assume that the assumption is valid in the entire RANS region.

In the remainder of this section we will demonstrate the SoS at the RANS/LES interface for two cases. The first case is an analysis of the flow state in the log layer, the second case is an *a posteriori* inspection of the flow states in the simulation of flow around a circular cylinder. The reason to investigate the log layer is mainly that an *a priori* analysis can be performed.

In the log layer the turbulent kinetic energy k is constant [19] and equal to $k = \tau_w/\rho\sqrt{\beta_k}$, where τ_w is the wall stress. Schlichting [14] gives the following engineering formula for the skin-friction coefficient for a flat plate: $C_f = \tau_w/\frac{1}{2}\rho U_{\text{ref}}^2 \approx 0.0576\text{Re}_x^{-1/5}$, where $\text{Re}_x = U_{\text{ref}}x/\nu$

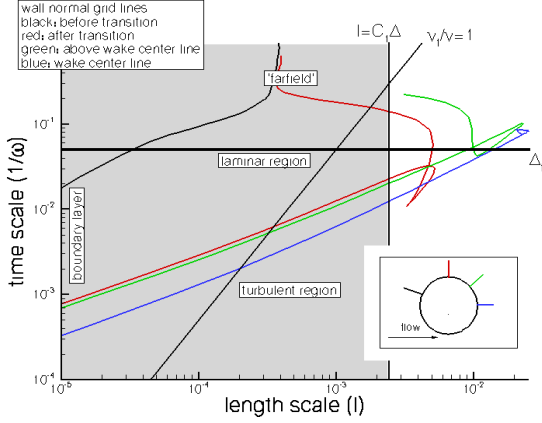


Fig. 1 Time-length scale plot at selected lines for the simulation of turbulent flow around a circular cylinder ($M = 0.3$ and $Re = 5 \cdot 10^4$).

is the Reynolds number based on the distance from the leading edge.

At the RANS/LES interface we have $l/U_{ref} = C_1 \Delta_t$. Assuming the interface to be located in the log layer, we have

$$\begin{aligned} \frac{1}{\omega} &= \frac{l}{\sqrt{k}} = \frac{l}{U_{ref}} \frac{U_{ref}}{\sqrt{k}} = C_1 \Delta_t \frac{U_{ref}}{\sqrt{k}} \\ &\approx C_1 \Delta_t \left(\frac{2\sqrt{\beta_k}}{0.0576} \right)^{\frac{1}{2}} Re_x^{\frac{1}{10}}. \end{aligned}$$

The dependence on Reynolds number is weak, and $Re_x^{1/10} < 4$ for Reynolds numbers up to one million. Given the constant $C_1 \approx 0.05$ we find $\frac{1}{\omega} < \Delta_t$, and hence the RANS time scale is less than the filter width, ensuring the SoS assumption.

Even though the RANS/LES interface could be located at the outer side of the log layer without violating the modeling assumptions, in general the interface will be located further away from the wall. In those regions the behaviour of the RANS time and length scales is not known *a priori*. A *posteriori* investigation of the scales is performed for the turbulent unsteady flow around a circular cylinder at $M_\infty = 0.3$ and $Re_\infty = 5 \cdot 10^4$, simulated with the RANS model. A periodic solution is obtained, and an instantaneous solution is examined.

In Figure 1 a length scale versus time scale plot is shown at selected wall-normal lines. The line locations are shown in the smaller figure: the

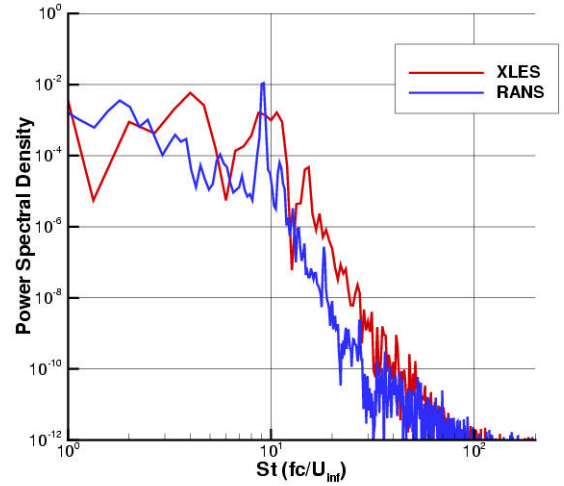


Fig. 2 Computational power density spectra of the normal force coefficient for the slender delta wing.

black line is before transition occurs, the red line just after transition, the green line is located in the turbulent wake, and the blue line is at the wake center line. All lines extend a cylinder radius into the domain. The left lower corner of the graph corresponds to the solution at the solid-wall. Also shown in the figure is the line where the turbulent viscosity is equal to the laminar viscosity, dividing the plot into a laminar region on the left and a turbulent region on the right (note that the black curve is located completely in the laminar region). As soon as the RANS length scale is equal to $C_1 \Delta$ the X-LES model would switch from RANS to LES mode (or vice-versa). In an X-LES simulation of the same flow a value of $C_1 = 0.05$ and a filter width of $0.05D$, where D is the cylinder diameter, is used [6]. The corresponding value $l = C_1 \Delta = 2.5 \cdot 10^{-3}$ at which the RANS/LES interface is located, is shown as a vertical line in the figure. The region left of this line, shaded in the figure, represents the region in RANS mode. The value of the time filter width, corresponding to the spatial filter width, is shown as a horizontal line.

Following the locus of the RANS time scale for, say, the red curve, coming from the solid wall, the transition is from RANS to LES and it is clear from the figure that at the interface the filter

width Δ_t is significantly greater than the RANS time scales.

3 Applications

3.1 Vortex breakdown for flight dynamics ¹

Subsonic flow around a half-span configuration of the ONERA 70-degree delta wing [8] is considered, with a Mach number $M_\infty = 0.069$, an angle of attack $\alpha = 27^\circ$, and a Reynolds number $Re_\infty = 1.56$ millions. The free-stream velocity U_o is 24 m/s. The delta wing has a flat surface on the leeward side where the leading-edge vortices are located. The wing root chord c is 950 mm.

Two simulations are performed. The first simulation solves the unsteady RANS equations combined with the TNT $k-\omega$ turbulence model. The turbulence model contains a correction to prevent excessive eddy viscosity levels in vortex cores typical for RANS models. More details on the simulation can be found in [15]. The second simulation is based on the X-LES model as described in Section 2.2. No vortex-core corrections are applied for the turbulence model, since the X-LES formulation is expected to have significantly lower eddy viscosity levels. In the X-LES simulation, the computational domain includes the wind-tunnel walls of the experiment [8].

Both simulations employ a baseline [10] time step $\Delta t = 0.0025c/U_0$. Figure 2 shows the power spectrum of the normal force coefficient. The figure shows a dominant peak for the RANS simulation corresponding to $St \approx 9$ ($f \approx 200\text{Hz}$). For the X-LES simulation the peak is not that dominant. It is clear from Figure 2 that the X-LES simulation displays increased power levels in the high frequency range, indicating that additional scales are being resolved compared to the RANS simulation.

Figure 3 shows the pressure-coefficient distributions at selected cross sections, two before, and two after breakdown. For both simulations, the suction peak of the primary vortex is evident. The

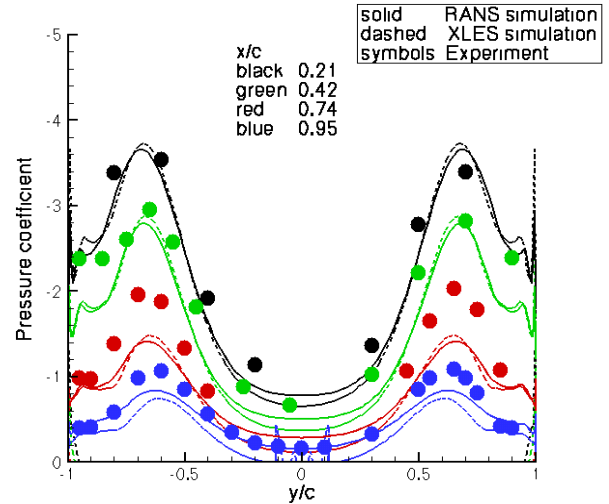


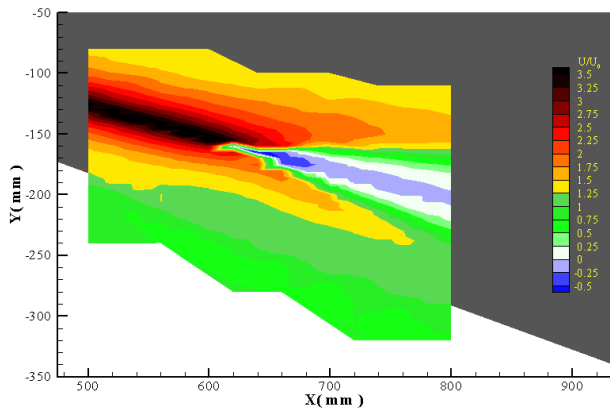
Fig. 3 Computational and experimental spanwise C_p distributions for the slender delta wing.

suction peaks of secondary vortices are slightly stronger for the X-LES simulation. Good agreement is shown up to 40% chord. Aft of this location, the computational suction peaks decrease rapidly in comparison to those of the experiment, for both the RANS and X-LES simulation. This discrepancy has consistently been found in other CFD simulations [9].

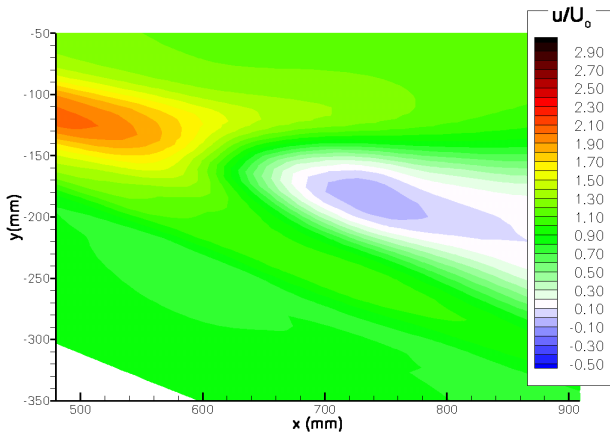
Figure 4 shows the axial velocity in a plane through the vortex core. The X-LES simulation displays a stronger vortex before breakdown and a significantly stronger recirculation at vortex breakdown than the RANS simulation. The vortex is not as strong as in the experiment. The RANS simulation predicts the vortex breakdown at $x/c \approx 0.74$. The X-LES simulation predicts the location at $x/c \approx 0.71$ which is closer to the experimental range of 60-71% chord. Accurate prediction of the vortex breakdown location is essential for the accurate prediction of the aerodynamic properties, such as the lift coefficient and the pitching moment coefficient, and their variation with aircraft attitude, which are basic inputs for the determination of departure susceptibility, departure motion and recovery from departure.

Figure 5 shows the cross-flow distributions of the axial vorticity component. The X-LES simulation gives an increase in vorticity level compared to the RANS results towards the experi-

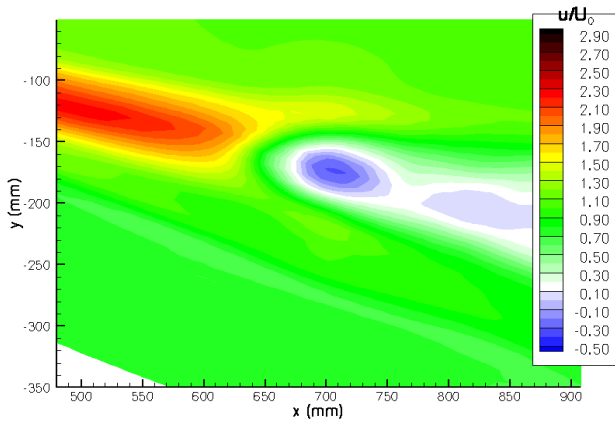
¹The work on the X-LES simulation has been executed within the framework of the DLR-NLR co-operation on hybrid RANS-LES modelling.



(a) experiment

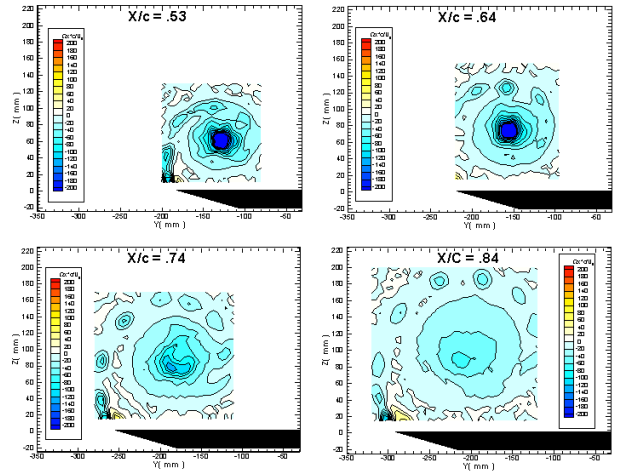


(b) RANS

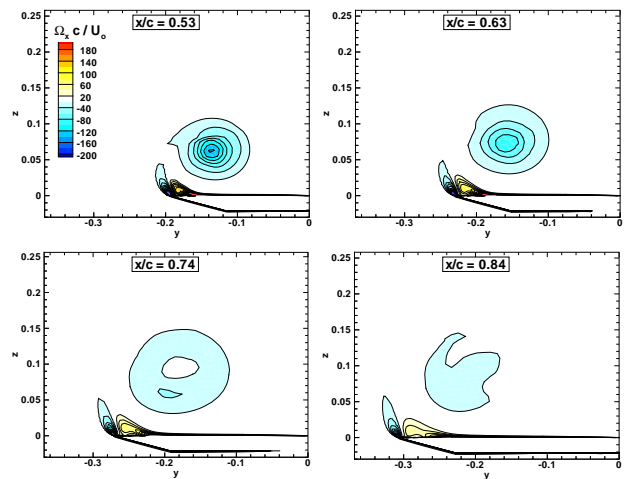


(c) X-LES

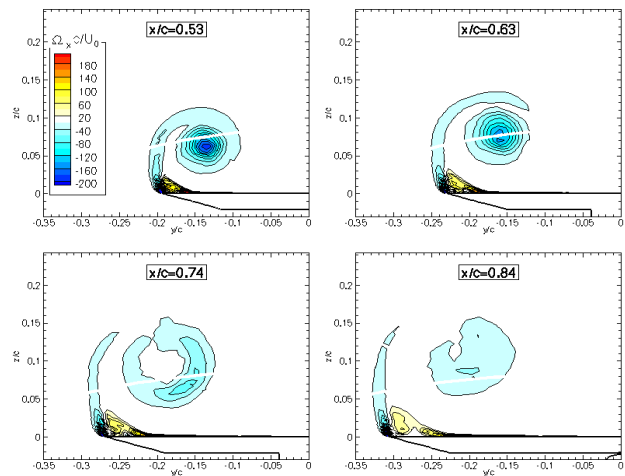
Fig. 4 Computational and experimental longitudinal distribution of the axial velocity for the slender delta wing.



(a) experiment



(b) RANS



(c) X-LES

Fig. 5 Computational crossflow distribution of the axial vorticity component for the slender delta wing.

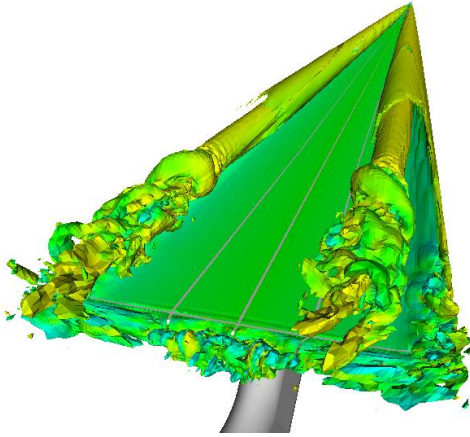


Fig. 6 Instantaneous computational vorticity distribution for the slender delta wing.

mental values, although the helical satellite structures are not resolved. A view of the complete vortex is shown in Figure 6, clearly showing the leading-edge vortex sheet before breakdown, and the turbulent structures after breakdown.

3.2 Aerodynamic loads for a generic space launcher²

To demonstrate the capability to compute dynamic loads on the nozzle of a space launcher, a generic space launcher model is used. The geometry is based on a ‘clean’ wind-tunnel model of scale 1:76.5, consisting of the space launcher, two side boosters, and the main nozzle, but excluding detailed protuberances such as cooling tubes (see Figure 7).

Simulations are performed at the following (wind-tunnel) conditions: a free-stream Mach number $M_\infty = 0.73$, a Reynolds number $Re_\infty = 6 \cdot 10^6$ based on a reference length $L = 0.5$ m, and zero angle of attack and side slip. Inside the boosters and the nozzle, the total pressure and total temperature are prescribed: $p_t = 27 p_{t,\infty}$ and $T_t = T_{t,\infty}$, and the velocity direction is set normal to the engine face.

The computations are performed on a 138-blocks grid with $4.78 \cdot 10^6$ grid cells. Separate

²The work has been conducted within NIVR contract number 49225N.

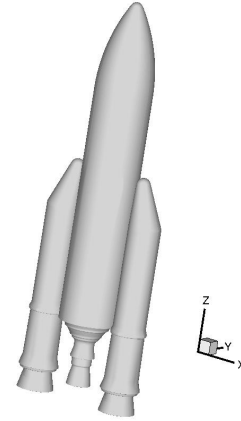


Fig. 7 Geometry of clean wind-tunnel model of scale 1:76.5 for the space launcher.

grid resolution requirements hold for the boundary layers (RANS mode) and the separated flow region around the nozzle (LES mode). The complete boundary layers are captured down to the viscous sublayer (wall distance of the first grid point of $y^+ \approx 1$). In the separated flow region, the mesh size is of the order $\Delta x \approx 6 \cdot 10^{-4}$ m. Roughly, this allows to capture the diameter of the largest vortices with 32 cells.

The resolved time span is determined by the lowest, dominant frequency that must be captured. In the wind-tunnel experiment, the Strouhal number of this frequency was found to be of the order 0.23 (based on the free-stream velocity and the base diameter). Simulations are performed for a length of time of six periods for this Strouhal number. This should be sufficient to get an impression of whether the relevant flow physics are captured. It is expected that for an accurate computation of statistical data more periods must be computed; typically up to 40 periods are suggested in the literature for hybrid RANS–LES simulations. Per period, 256 time steps are taken, resulting in a time step $\Delta t = 0.0024L/u_\infty$. This implies a Courant number in the separated flow region of order 2.

In Figure 8 an instantaneous plot of the pressure coefficient in the symmetry plane is shown. Rich flow details demonstrate the capability of X-LES to capture small flow structures.

In order to obtain an appreciation of the computed dynamic aerodynamic data, the Power

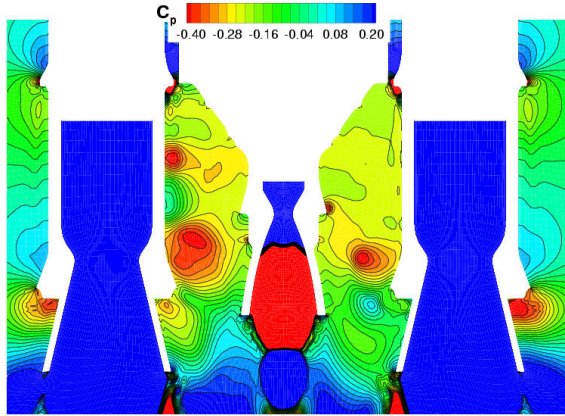
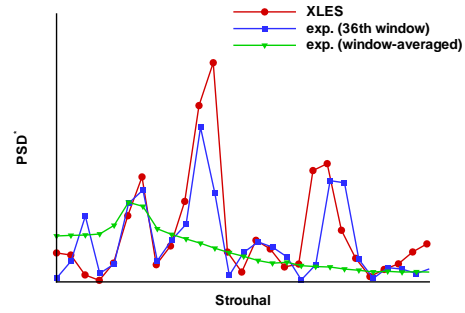
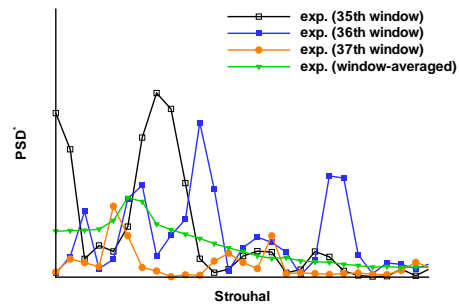


Fig. 8 Final contours of the pressure coefficient C_p on the x - z symmetry plane of the space launcher.

Spectral Density (PSD) of the pressure is computed at a single location on the nozzle, and compared to experimental wind-tunnel data, obtained in de DNW-HST wind-tunnel, around a geometrically more complex model. It should be emphasized that the experimental data are used only for a qualitative assessment, since there are essential differences between the computational and the experimental case. For a meaningful comparison, the PSD's should be computed for the same length of (non-dimensional) time. As the X-LES computation spans only a fraction of the time of the experiment, the PSD's are based on the time span of the computation. There are then 256 windows available from the experiment, spanning the same length of time, for each of which the PSD can be computed. Figure 9(a) compares the PSD of the X-LES computation with the PSD of the 36th window of the experiment, which is found to give a minimum deviation between the two. The agreement is remarkably close, but this should only be interpreted as that the computational and experimental results have comparable frequency contents in the selected window. To stress this point, Figure 9(b) shows a window-to-window variation, which is quite significant. Nonetheless, there is a strong indication that the numerical algorithm is capable of capturing typical dynamic flow physics observed in the experiment.



(a) Computational and experimental spectra



(b) Window-wise variation of experimental spectra

Fig. 9 Power Spectral Densities at a location on the nozzle of the space launcher.

4 Conclusions

For various aerospace applications accurate characterisation of dynamic flow phenomena is required for several reasons explained in the paper. Two examples of such flows have been treated in this paper, using a new Extra-large Eddy Simulation method especially designed for massively separated flow.

The X-LES model is a non-zonal method that uses a single formulation in the entire flow domain. A theoretical foundation, based on time filtering, for this method has been presented. RANS turbulence models are applied in those regions of the flow where the assumption of separation of scales is valid, and LES turbulence models otherwise.

The X-LES model has been applied to the vortex breakdown over a slender delta wing, and the computation of an external load case on the nozzle of a generic space launcher. Compared to

RANS simulations, the X-LES simulations show clear qualitative improvement, since more flow details are resolved. Comparison with experiment suggests that the X-LES model is capable of solving the same physical phenomena. For the vortex breakdown application, X-LES improves the strength of the breakdown, in terms of recirculation, compared to the RANS simulation. More quantitative comparison with experiments requires statistically converged solutions, which are not yet obtained for the two applications.

In conclusion, the X-LES model provides an excellent starting point for the prediction of highly dynamic flows. Ongoing research is focused on more efficient time integration schemes.

References

- [1] S. B. Anderson. Handling qualities related to stall/spin accidents of supersonic fighter aircraft. *J. Aircraft*, 22(10):875–880, 1985.
- [2] W. Bihrlé and B. Barnhart. Departure susceptibility and uncoordinated roll-reversal boundaries for fighter configurations. *J. Aircraft*, 19(11):897–903, 1982.
- [3] E. F. Charlton. *Numerical stability and control analysis towards falling-leaf prediction capabilities of Splitflow for two generic high-performance aircraft models*. NASA CR-1998-208730, 1998.
- [4] S. Cook, J. Chambers, A. Kokolios, R. Niewoehner, D. Owens, and M. Roesch. An integrated approach to assessment of abrupt wing stall for advanced aircraft. *AIAA paper*, 2003-0926, 2003.
- [5] G.W. Ryan III. A genetic search technique for identification of aircraft departures. Technical Report CR-4688, NASA, 1995.
- [6] J. C. Kok, H. S. Dol, B. Oskam, and H. van der Ven. Extra-large eddy simulation of massively separated flows. *AIAA paper*, 2004-264, 2004.
- [7] N. McMillin, R. Hall, and J. Lamar. Transonic experimental observations of abrupt wing stall on an F/A-18E model. *AIAA paper*, 2003-0591, 2003.
- [8] A. M. Mitchell. *Caractérisation et contrôle de l'éclatement tourbillonnaire sur une aile delta aux hautes incidences*. Ph.D dissertation, Université Paris VI, 2000.
- [9] Anthony M. Mitchell, Scott A. Morton, Xing Z. Huang, and Niek G. Verhaagen. NATO RTO Task Group-080 “Vortex breakdown over slender wings” validation and verification, conclusions and recommendations. *AIAA paper*, 2003-4218, 2003.
- [10] Scott A. Morton, James Forsythe, Anthony Mitchell, and David Hajek. DES and RANS simulations of delta wing vortical flows. *AIAA paper*, 2002-0587, 2002.
- [11] R.C. Nelson and P. Alain. The unsteady aerodynamics of slender wings and aircraft undergoing large amplitude maneuvers. *Progress in Aerospace Sciences*, 39:185–248, 2003.
- [12] L.T. Nguyen and J.V. Foster. Development of a preliminary high-angle-of-attack nose-down pitch control requirement for high-performance aircraft. Technical Report TM-101684, NASA, 1990.
- [13] C. David Pruett. Eulerian time-domain filtering for spatial large-eddy simulation. *AIAA Journal*, 38:1634–1642, 2000.
- [14] H. Schlichting. *Boundary-Layer Theory*. McGraw-Hill, New York, 1968.
- [15] B.I. Soemarwoto and O.J. Boelens. Simulation of vortical flow over a slender delta wing experiencing vortex breakdown. Technical Report TP-2003-396, also AIAA-2003-4215, NLR, 2003.
- [16] B.I. Soemarwoto, B.B. Prananta, and O.J. Boelens. Towards high-fidelity flight dynamic assessment of high performance fighter aircraft. *presented at the sixth Onera-DLR Aerospace Symposium, June 22-23, 2004, Berlin*, 2004.
- [17] P.R. Spalart. Strategies for turbulence modelling and simulations. *Int. J. Heat Fluid Flow*, 21:252–263, 2000.
- [18] R. Weismann. Preliminary criteria for predicting departure characteristics/spin susceptibility of fighter-type aircraft. *J. Aircraft*, 10:214–219, 1973.
- [19] D.C. Wilcox. *Turbulence Modeling for CFD*. DCW Industries, Inc., 2nd edition, 1998.
- [20] S. Woodson, B. Green, J. Chung, D. Grove, P. Parikh, and J. Forsythe. Understanding abrupt wing stall with cfd. *AIAA paper*, 2003-0592, 2003.